Modelling fluid flow in complex natural fault zones: Implications for natural and human-induced earthquake nucleation

Thomas Snell [a], Nicola De Paola [a,*], Jeroen van Hunen [a], Stefan Nielsen [a], Cristiano Collettini [b]

[a] *Department of Earth Sciences, Durham University, Durham, DH13LE, United Kingdom*
[b] *Dipartimento di Scienze della Terra, Sapienza Università di Roma, 00185, Roma, Italy*

A B S T R A C T

Pore fluid overpressures in active fault systems can drive fluid flow and cause fault weakening and seismicity. In return, deformation accommodated by different modes of failure (e.g. brittle vs. ductile) also affects fault zone permeability and, hence, fluid flow and pore fluid pressure distribution. Current numerical simulation techniques model how fluid flow controls fault reactivation and associated seismicity. However, the control exerted by pore fluid pressure on the transition from slow aseismic fault sliding to fast seismic sliding, during the earthquake nucleation phase, is still poorly understood. Here, we model overpressured, supercritical CO_2 fluid flow in natural faults, where non-linear, complex feedback between fluid flow, fluid pressure and fault deformation controls the length of the nucleation phase of an earthquake and the duration of the interseismic period. The model setup is an analogue for recent seismic source events in the Northern Apennines of Italy (e.g. M_w 6.0 1997-98 Colfiorito and M_w 6.5 2016 Norcia earthquakes). Our modelling results of Darcy fluid flow show that the duration of the nucleation phase can be reduced by orders of magnitude, when realistic models of fault zone architecture and pore pressure- and deformation-dependent permeability are considered. In particular, earthquake nucleation phase duration can drop from more than 10 years to a few days/minutes, while the seismic moment can decrease by a factor of 6. Notably, the moment of aseismic slip ($M_0 = 10^9$ N m) obtained during the nucleation phase modelled in our study is of the same order as the detection limit of local strain measurements using strain meters. These findings have significant implications for earthquake early warning systems, as the duration and moment of the nucleation phase will affect the likelihood of timely precursory signal detection. Interestingly, aseismic slip has been measured up to a few months before some recent large earthquakes, although in a different tectonic context than the model developed here, rekindling interest in the nucleation phase of earthquakes. In addition, our results have important implications for short and long term earthquake forecasting, as crustal fluid migration during the interseismic period may control fault strength and earthquake recurrence intervals.

© 2019 The Author(s). Published by Elsevier B.V. This is an open access article under the CC BY license (http://creativecommons.org/licenses/by/4.0/).

1. Introduction

Pore fluid pressure plays a primary mechanical role during faulting as it reduces the frictional fault strength (Cox, 2010; Sibson, 1992). There is strong geological, geophysical and experimental evidence that fluid migration in the upper crust controls faulting (Sibson, 2000), and natural (Di Luccio et al., 2010; Miller et al., 2004) and human induced (Ellsworth, 2013; McGarr et al., 2015; Scuderi and Collettini, 2016; Scuderi et al., 2017) seismic activity.

Fluid circulation within the upper crust is strongly dependent on the transport properties of rocks (i.e., permeability). Rock permeability and porosity vary with pressure conditions and deformation (Paterson and Wong, 2005), which control the development and connectivity of fracture patterns across a range of scales (Caine et al., 1996; De Paola et al., 2009; Mitchell and Faulkner, 2008; Peach and Spiers, 1996; Wong et al., 1997; Zoback and Byerlee, 1975).

In previous modelling efforts, the link between fluid flow and faulting has been investigated using coupled deformation and fluid flow modelling (Cappa and Rutqvist, 2012, 2011, Rutqvist et al., 2015, 2013). Coupled fluid flow and geomechanical fault slip (e.g. fault reactivation) analysis have been used, for example, to model the spatial evolution of both in situ stresses and fluid pressure,

to estimate the maximum sustainable injection pressure during geological sequestration of CO_2 (Rutqvist et al., 2007). In these studies, fluid flow was modelled for metre to kilometre scale fault zone features, considering permeability as a continuous function of porosity, volumetric strain, average effective stress, and fault shear strain. This approach has been extended to also include the effect of simplistic fault zone architectures (Cappa et al., 2009; Cappa and Rutqvist, 2011; Leclère et al., 2015; Rinaldi et al., 2014; Rutqvist et al., 2013). Overall, previous results cited above show that pressure increase due to shear-enhanced permeability plays an important role, as it can facilitate the propagation of fault instability and extend permeability enhancement through the overlying caprock.

Here, we model fluid flow in exhumed (>1 km depth), large displacement (>100 m) faults in evaporite sequences with complex architecture, and pore pressure- and deformation-dependent permeability (De Paola et al., 2008; Collettini et al., 2009). These faults represent an analogue of the seismic sources at hypocentre depth of recent seismic events in the Northern Apennines of Italy (e.g. M_w 6.0 1997-98 Colfiorito and M_w 6.5 2016 Norcia earthquakes). Modelled fluid flow is then used to investigate the effects of pore fluid pressure distribution during the nucleation phase that precedes an earthquake.

Identifying the factors that control the duration of the nucleation phase of earthquakes has significant implications for earthquake early warning systems, as the duration of the nucleation phase will affect the likelihood of timely precursory signal detection. Furthermore, modelling pore fluid pressure evolution during the interseismic period has relevant implications for long term earthquake forecasting, as it controls fault strength and earthquake recurrence intervals.

2. Numerical method

We perform numerical simulations to model fluid flow in fault zones with realistic, complex fault zone architecture. In our model, fault zone permeability is assumed to vary as a function of effective pressure and mode of failure (e.g. brittle and localised vs. ductile and distributed), during the interseismic and preseismic period. Modelled fluid flow during the pre-seismic period is used to investigate the effects of pore fluid pressure distribution during the nucleation phase that precedes an earthquake.

2.1. Porous media flow and numerical solution

We develop an approach based on the diffusion of pore pressure within a classical porous medium using

$$\frac{dP}{dt} = \frac{\nabla \cdot (k \nabla P)}{\beta \eta \varphi}, \tag{1}$$

which relates pore pressure P and permeability k to the rate of change of pressure with time t. All symbols and values used are explained in Table 1. The compressibility β is approximated as being only the fluid compressibility, because the compressibility of supercritical CO_2 exceeds that of evaporite rocks by several orders of magnitude (Burke, 2011). It is also assumed that the variation of fluid viscosity η and compressibility with effective pressure is negligible for the range of conditions simulated (Burke, 2011), where effective pressure is defined by

$$P_e = \sigma_L - P, \tag{2}$$

where σ_L is the lithostatic load and P the pore pressure.

Following the experimental permeability relations observed in low porosity evaporite rocks (De Paola et al., 2009; see section 2.2.3 below), we consider that the solid rock is an ideal porous medium. Its permeability can be expressed as a function of effective pressure in the presence of ductile deformations, accommodated by small, distributed fracture patterns (Detournay and Cheng, 1993). We also consider singularities in the time derivative of permeability when localised brittle failure occurs, assuming instantaneous increase of permeability within the fault (De Paola et al., 2009).

We make the simplifying assumption that the modelled fault zone is saturated with supercritical CO_2 and can be treated as being a single phase. This assumption is in accord with field data supporting large CO_2 fluxes in the epicentre areas of the Northern Apennines seismic belt (e.g. M_w 6.0 1997-98 Colfiorito and M_w 6.3 2009 L'Aquila extensional earthquakes), where large deep-seated CO_2 flux greater than 0.45 t day^{-1} km^{-2} have been measured (Chiodini et al., 2004; Collettini et al., 2008).

Although fault zone geometries, physical properties and mechanical behaviour used in our modelling are inferred and constrained from main seismic extensional fault zone in evaporite rocks (Collettini et al., 2009; De Paola et al., 2009, 2008), the methods can be generalised and applied to any natural fault zone with known fault zone architecture and constrained physical and mechanical properties.

The nonlinear fluid pressure diffusion (Eq. (1)) and resulting pore fluid flow are discretised using a finite difference numerical solution method, and implemented in a custom-built Matlab code. The stiff set of equations underpinning the nonlinearity of the pore pressure diffusion simulations tends to give rise to numerical instability with most standard solvers. Here, we exploit the robust convergence behaviour of the Matlab function ODE23tb. Further details on the implementation and validation of the numerical model are provided in the Supplementary Material, sections II and III.

2.2. Model input parameters

2.2.1. Fault zone architecture

The modelled fault zones formed within the Triassic Evaporite formation; a 1.5–2 km thick sequence of 6–19 m interbedded anhydrite/gypsum and dolostones (Barchi, 2002; Trippetta et al., 2013). Seismological data and observations from hypocentre depths in the Northern Apennines seismic belt indicate the presence of shallow dipping (45°) faults, which may require the generation of fluid overpressure leading to fault reactivation (Barchi, 2002; Miller et al., 2004; Mirabella et al., 2008).

Fault zone architecture is constrained by field observations reporting an about 5 m wide fault core, where most of the slip accommodated by the fault is localised (Fig. 1a; Collettini et al., 2009; De Paola et al., 2008). Outside the fault core, a well-developed damage zone (DZ) is observed within thick (up to twenty meters) fractured dolostones, extending for tens of metres in either direction from the fault core. Conversely, no macroscopic fracturing is observed within the foliated anhydrite layer immediately adjacent to the fault core, on either side of the fractured dolostones (Fig. 1a) (De Paola et al., 2008).

The fault core shows a complex structure, with a 1 m wide inner fault core (IFC) domain, containing fine-grained cohesive cataclasites, which is enclosed on both sides by 2 m wide outer fault core (OFC) domains (Fig. 1b), containing cohesive and continuous foliated anhydrites, which are not fractured, and lenses of fractured dolomite dispersed within the foliated anhydrites (De Paola et al., 2008). Within the IFC, slip is further localised along straight principal slip surfaces (PSS), which are located within thin (millimetre-scale) principal slip zones (PSZ) of ultra fine-grained incohesive anhydrite and dolomite-rich gouges (Fig. 1b) (De Paola et al., 2008).

Table 1
Physical constants and variables used in simulations.

Symbol	Definition	Value	Reference
Fluid Properties			
β	Compressibility	10^{-10} Pa^{-1}	1
η	Fluid viscosity	10^{-5} Pa s	1
p	Pressure	–	–
p_e	Effective pressure	–	–
t	Time	–	–
Fault Properties			
ϕ	Porosity	0%	2
μ_S	Static friction of the fault plane (Primary slip zone)	0.6	3
G	Shear modulus	45.7 Gpa	4
D_C	Critical slip distance	63 μm	5
F	Difference of the rate and state parameters	0.003	5
ξ	Failure patch geometry factor	1	–
L_{OFC}	Outer fault core width	2 m	–
L_{IFC}	Inner fault core width	1 m	–
L_{PSZ}	Primary slip zone width	2 mm	–
C_{fault}	Fault cohesion (Primary slip zone)	0	–
$\mu_{OFC\text{-}brittle}$	Internal friction of the OFC (brittle)	0.704	2
$C_{OFC\text{-}brittle}$	Cohesion of the OFC (brittle)	15.5 MPa	2
$\mu_{OFC\text{-}ductile}$	Internal friction of the OFC (ductile)	0	2
$C_{OFC\text{-}ductile}$	Cohesion of the OFC (ductile)	38.14 MPa	2
L_N	Nucleation length	–	–
σ_N	Normal stress	–	–
σ'_N	Effective normal stress	–	–
σ_1	Principal maximum stress	–	–
σ_3	Principal minimum stress	–	–
τ	Shear stress	–	–
τ_f	Shear strength	–	–
T_R	Tectonic loading rate	0.15 MPa yr^{-1}	–
Permeability Properties			
$k_{\perp OFC\text{-}prefailure}$	Unstressed prefailure permeability of the OFC	8×10^{-21} m^2	2
$k_{\perp OFC\text{-}brittle}$	Unstressed permeability of the OFC after brittle failure	1.1287×10^{-18} m^2	2
$k_{\perp OFC\text{-}ductile}$	Unstressed permeability of the OFC after ductile failure	2.407×10^{-18} m^2	2
$k_{\perp IFC}$	IFC permeability	10^{-19} m^2	6
$k_{\perp PSZ}$	PSZ permeability	10^{-21} m^2	7
$\gamma_{\perp OFC\text{ - }prefailure}$	OFC prefailure pressure sensitivity	-0.04 Mpa^{-1}	2
$\gamma_{\perp OFC\text{ - }brittle}$	OFC pressure sensitivity after brittle failure	0	2
$\gamma_{\perp OFC\text{ - }ductile}$	OFC pressure sensitivity after ductile failure	-0.1136 Mpa^{-1}	2
$k_{\parallel OFC\text{-}prefailure}$	Unstressed prefailure permeability of the OFC	3×10^{-19} m^2	2
$k_{\parallel OFC\text{-}brittle}$	Unstressed permeability of the OFC after brittle failure	1.39×10^{-17} m^2	2
$k_{\parallel OFC\text{-}ductile}$	Unstressed permeability of the OFC after ductile failure	3.681×10^{-17} m^2	2
$k_{\parallel IFC}$	IFC permeability	10^{-17} m^2	6
$k_{\parallel PSZ}$	PSZ permeability	10^{-19} m^2	7
$\gamma_{\parallel OFC\text{ - }prefailure}$	OFC prefailure pressure sensitivity	-0.13 Mpa^{-1}	2
$\gamma_{\parallel OFC\text{ - }brittle}$	OFC pressure sensitivity after brittle failure	0	2
$\gamma_{\parallel OFC\text{ - }ductile}$	OFC pressure sensitivity after ductile failure	-0.07968 Mpa^{-1}	2
k	Permeability tensor	–	–

OFC = Outer Fault Core
IFC = Inner Fault Core
PSZ = Primary Slip Zone

References

1: Burke, 2011
2: De Paola et al., 2009
3: Byerlee, 1978
4: Anderson and Isaak, 1995
5: Scuderi et al., 2013
6: Evans et al., 1997
7: Wibberley and Shimamoto, 2002

A schematic, yet realistic, fault zone architecture is used within the model (Fig. 2), where it is assumed that seismic slip occurs along a single PSZ of zero thickness, made of incohesive fault gouges and located in the centre of the IFC, which is made of cohesive cataclasites (Fig. 2).

2.2.2. Failure envelopes

The failure envelopes, mode of failure and transport properties of rocks within the OFC and IFC fault zone domains have been obtained from triaxial deformation experiments with fluid flow, performed on borehole samples of Triassic Evaporites rocks (De Paola et al., 2009).

The strength of intact anhydrite rocks is controlled by the presence and orientation of fabric anisotropy, with the weakest rocks being those where foliation is sub-parallel to the loading direction. On the other hand, the transition between localised brittle to distributed ductile mode of failure is controlled by effective pressures, and occurs at about 20 MPa regardless of grain size, presence of fabric anisotropy and its orientation (De Paola et al., 2009).
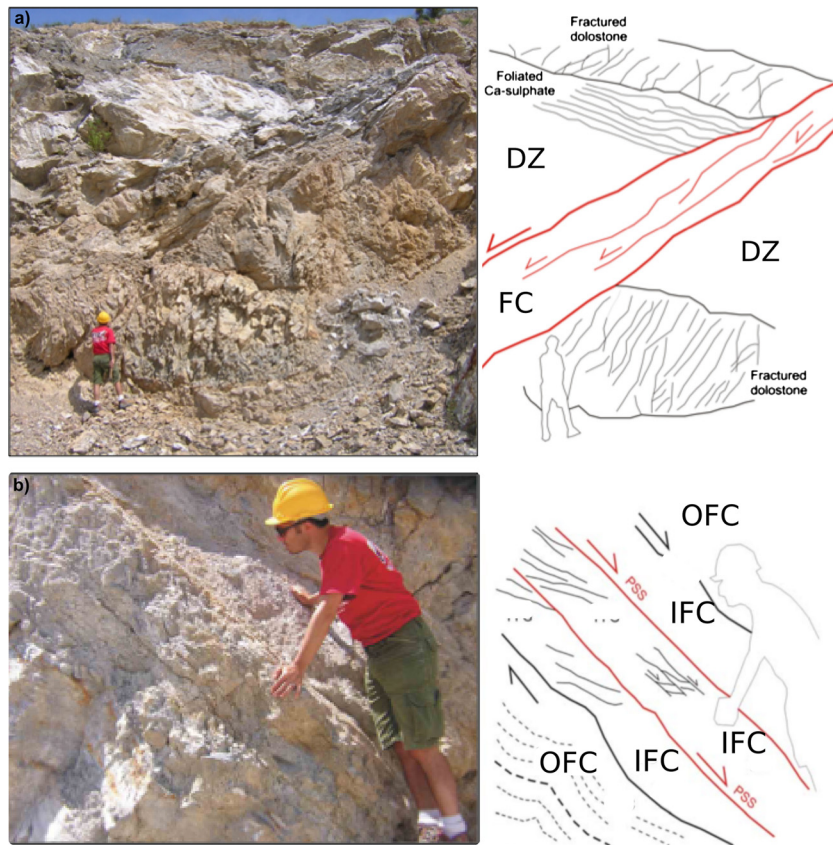
Fig. 1. The Roccastrada fault, which is an exhumed analogue to the hypocentre fault of the 1997-98 Colfiorito seismic sequence. (a) Outcrop scale normal fault zone within the Triassic Evaporites and line drawing highlighting the fault zone structure, showing the sharp boundary between the fault core rocks (FC) and the fractured dolostones and foliated anhydrites in the damage zone (DZ). (b) A large-scale view of shear zone's IFC with a line drawing of the internal structure: IFCB (inner fault core boundary), PSS (principal slip surface), FG (fault gouge), FFG (foliated fault gouge), FFC (foliated fault core).
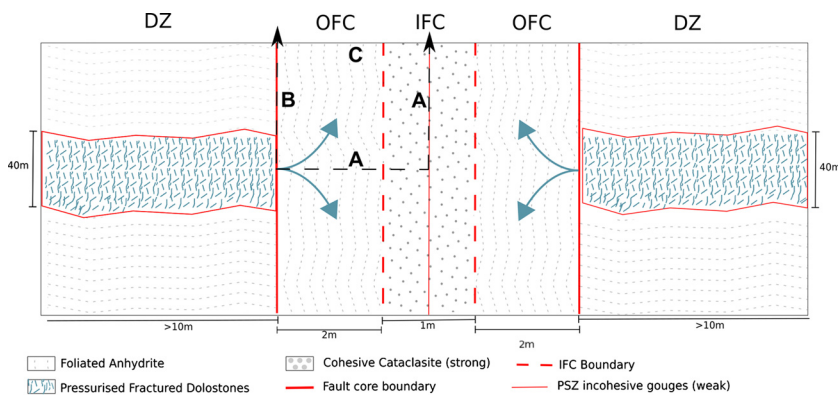

Fig. 2. Idealised fault zone architecture used within the model. Schematics of fault zone domains damage zone (DZ), outer fault core (OFC) and inner fault core (IFC) considered for the numerical simulations in this study. The simulations have been run at a reference 7 km depth, for a fault dipping at 45° to the horizontal, with the maximum principal stress σ_1 which is vertical and assumed at an angle of 45° to the fault. The directly simulated area is shown in the black dashed box, with modelling boundary conditions indicated by the letters A (symmetry boundary, fluid conditions are identical on either side so no flow perpendicular to boundary), B (fixed pressure due to high permeability in DZ, overpressure at contact with pressurised dolostones, and hydrostatic pressure at contact with foliated anyhydrite) and C (a fixed hydrostatic pressure boundary 1000 m above lowest symmetry boundary, sufficiently removed so that pressure perturbations have decayed by this point).

Mohr-Coulomb failure envelopes have been constructed for each fault zone domain, i.e. the OFC, the IFC and the PSZ (Fig. 3). The failure envelope of the foliated anhydrite in the OFC is obtained from triaxial loading experiments performed on anhydrite borehole samples with foliation oriented sub-parallel to the loading direction (Fig. 3a; De Paola et al., 2009). A sharp transition from localised brittle to distributed ductile mode of failure is observed at effective pressures of about 20 MPa (Fig. 3a). The failure envelope of the IFC, made of cohesive, anhydrite bearing fine-grained cataclasites, with no fabric, is assumed from triaxial load-

ing experiments performed on fine-grained, homogeneous anhydrite borehole samples (Fig. 3a; De Paola et al., 2009). The failure envelope of the PSZ – the actively slipping plane within the IFC – is assumed consistent to that of a cohesionless fault plane, with Byerlee's sliding friction coefficient of 0.6 (Fig. 3b; Scuderi et al., 2013).

In our simulations, the frictional properties of the fault are assumed homogeneous. However, fault strength inhomogeneity is induced by the variations of fluid pressure along the fault, due to fault strength dependence on effective normal stress.
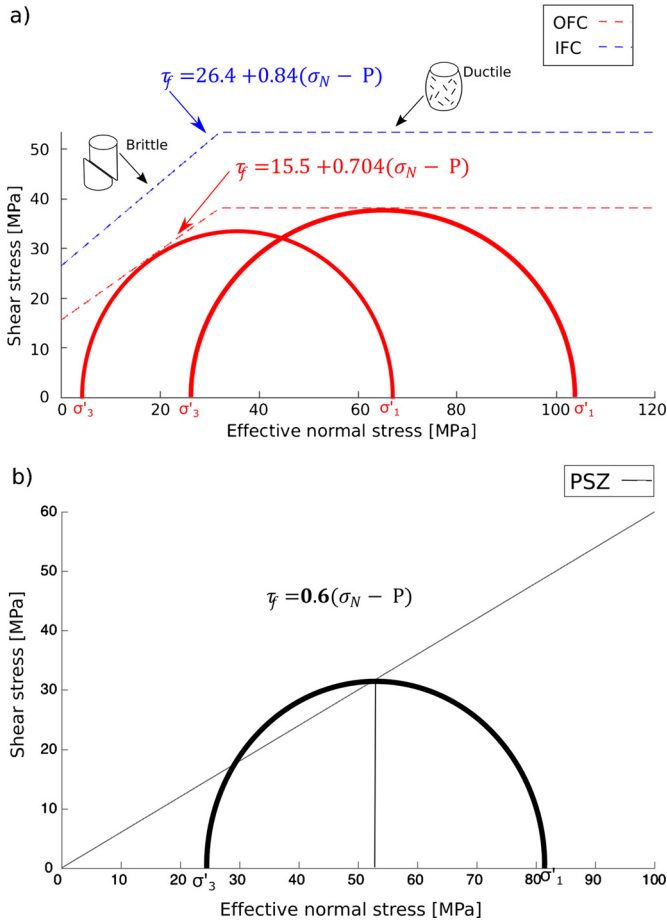
Fig. 3. Failure envelopes and schematic Mohr circles for the different fault zone domains: a) The brittle (localised deformation) and ductile (distributed failure) regions of the OFC and IFC failure envelopes are indicated with core plug sketches. The schematic Mohr circles show the onset of brittle and ductile failure in the OFC, respectively. b) The Mohr circle shows the onset of frictional sliding along a cohesionless principal slip surface within the PSZ (black line within the Mohr circle).

2.2.3. Model of pre-seismic nucleation growth

During the nucleation stage of an earthquake, stable sliding spreads out from an initial small fault patch (L_F) until it reaches a critical size, the nucleation length (L_N), at which unstable fast sliding begins causing the propagation of the rupture (Marone, 1998; Scholz, 1998).

In our model, frictional sliding will initiate on any portion of the fault (L_F) where the shear stress is equal to the fault strength defined by the Coulomb failure criterion. The failure patch L_F is assumed to undergo stable sliding when it is smaller than the nucleation length L_N. Within the failure patch (L_F), stress cannot rise above the frictional sliding value, and any additional load after failure will be released through sliding. However, because the failure patch is smaller than the nucleation length, no significant slip acceleration will occur, and the frictional level will not be significantly affected if it obeys rate-and-state dependent friction. The failure patch length (L_F) will gradually grow in time, as larger portion of the fault attain the fault strength values, because of the shear stress increase due to constant tectonic load and to fault strength reduction due to fluid pressure diffusion. However, failure patch (L_F) will not undergo spontaneous growth until the nucleation length L_N has been reached. In our model, we define the nucleation process as the quasi-static growth of the failure patch L_F, until it reaches the nucleation length L_N and the seismic instability phase would initiate. Note that during the quasi-static growth, we do not compute the stress transfer from the failure patch into

its vicinity. Such stress variation is implicitly accounted for in the definition of critical length L_N, therefore it has no significant effect on the stability of the incipient rupture during the nucleation phase. However, stress transfer may induce local variations in the stress-sensitive permeability, and such local variations we do not account for in our model. Furthermore, the investigation of the dynamic evolution of the seismic rupture phase is beyond the point of this study and our simulations end when L_N is reached.

In the framework of rate-and-state friction theory, the critical patch size or nucleation length is inversely proportional to the effective normal stress (Campillo et al., 2001; Scholz, 1998) and can be defined as

$$L_N = \frac{\xi G D_C}{F \sigma'_N}, \tag{3}$$

where ξ, is a geometric factor that can be approximated to 1, G is the shear modulus, D_C is the critical slip distance and F is the difference of the rate and state parameters $b - a$, and σ'_N is the effective normal stress. We compute the nucleation length L_N at any given time as a function of the evolving modelled pore pressure according to Eq. (3). Hence, modelling results of pore pressure evolution can be used to investigate the evolution in space and time of the nucleation length, during the nucleation stage.

To compute the nucleation length L_N we use the highest value of normal stress within the patch L_F (stiffest point within L_F); this results in a good approximation of the actual nucleation length as demonstrated in Campillo et al. (2001) and Uenishi and Rice (2003).

The seismic moment M_0 released by the failure patch L_F during the whole nucleation phase can be approximately calculated (full details given in Supplementary Materials – Section I), up to the point where the size L_N of the nucleation length is reached and seismic slip starts, as $M_o = uG\pi 4L_N^2$, assuming a circular patch of diameter L_F. The preseismic slip u can be obtained as $u = \frac{16}{7\pi}\frac{\Delta\tau}{G}L_N$, where $\Delta\tau$ corresponds to the stress drop $\Delta\tau = \frac{\sigma_1 - \sigma_3}{2} \cos\cos 45°$.

2.2.4. Fault zone transport properties

The permeability tensor relations have been constructed for the OFC using available data from triaxial deformation experiments with fluid flow (De Paola et al., 2009). In particular, the fault parallel and perpendicular components of the permeability tensor in the OFC are obtained from loading experiments to failure with fluid flow imposed parallel and perpendicular to fabric, respectively (De Paola et al., 2009). To a first approximation, laboratory experiments show that the permeability of anhydrite rocks before failure are controlled by the combined effect of: 1) effective pressure, as permeability decreases with increasing effective pressure, due to porosity reduction (Fig. 4a-b); and 2) deformation, as permeability increases with increasing loading due to the creation of fractures within the rock (Fig. 4c-d). For a given value of pore pressure, a sudden increase in permeability is observed at failure, and its magnitude is controlled by the brittle and ductile mode of failure (Fig. 4c-d), respectively.

The pore pressure sensitivity of permeability k is described by the general, experimentally derived, empirical equation

$$k = k_0 \exp(-\gamma P_e), \tag{4}$$

where P_e is the effective pressure, k_0 is the reference permeability at an effective pressure of zero and γ is the pressure sensitivity coefficient. At the onset of distributed ductile failure, permeability will rapidly increase (Fig. 4c-d). Then, for a given value of effective pressure during ductile failure, permeability will reach a plateau value when a percolation threshold state is attained in the sample, due to the development of a fully connected network of
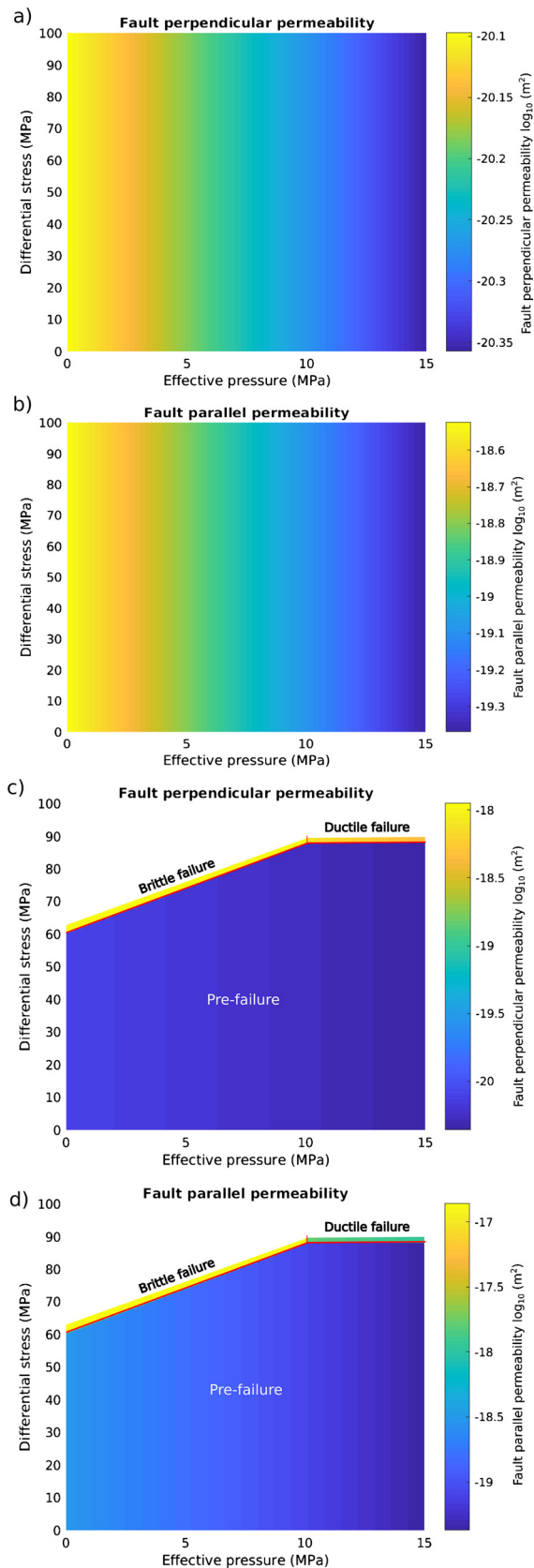
Fig. 4. Log-plot of permeability against effective normal stress and shear stress based on triaxial experiments performed on OFC Triassic Evaporites samples (After De Paola et al., 2009). a–b) Fault parallel (a) and fault perpendicular (b) permeability evolution with effective pore pressure derived from static triaxial experiments with no loading of the sample. c–d) Fault parallel (c) and fault perpendicular (d) permeability evolution with effective pore pressure and stress dependence obtained during dynamic triaxial experiments, when samples are loaded to failure.

microfractures (Fig. 4c-d; De Paola et al., 2009). Permeability of samples deforming in a ductile mode is sensitive to effective pressure variations (Fig. 4c-d; Table 1), which can reduce or enhance the porosity of the sample by closing or opening fractures, respectively (De Paola et al., 2009).

Conversely, at the onset of localised brittle failure, permeability will rapidly increase to a relatively high value (Fig. 4c-d). After the occurrence of brittle failure, we assume that permeability will not be sensitive to effective pressure variations (Fig. 4c-d; Table 1), as the macroscopic fault/fracture can act as an effective conduit for fluid migration (De Paola et al., 2009). We also assume that all fractures created during the pre- and co-seismic phase will be fully healed soon after the main seismic event. This is due to the efficiency of hydrothermal healing processes, acting during the interseismic period, which may seal micro- and macro-scale fractures within a few years of a slip event (Pluymakers and Spiers, 2015).

The permeability of the fine-grained cataclasites in the IFC and gouges in the PSZ are assumed to be anisotropic in the fault-parallel and fault-orthogonal direction (Evans et al., 1997; Wibberley and Shimamoto, 2002), but otherwise in the OFC, they are not assumed to depend on pore pressure and deformation (Table 1).

2.3. Model setup

The model setup assumes that pore fluid overpressure within the damage zone (DZ) is largely contained within the fractured dolostone layer (Fig. 2). Hydrostatic pore fluid pressure occurs within the layers of foliated anhydrite in the DZ, which act as a perfect seal at their contacts immediately above and below the overpressured dolostone reservoir (Fig. 2). The initial pore pressure distribution within the fault core is assumed to be uniform and hydrostatic. This is due to any overpressure build-up within the fault core being quickly released during the interseismic period or soon after the seismic event (Miller et al., 2004) by fracturing of the hydraulic barrier (i.e. fault-valve behaviour; Sibson, 1992).

We simulate an area of 2.5 by 1000 m, representing the upper left quadrant of the fault core (Fig. 2), located at a hypocentre model depth of 7 km and subject to extensional tectonic loading by reduction of the least principal stress axis at a rate of 0.15 MPa/yr, based on the extensional tectonic setting (Chiaraluce et al., 2003). The simulations have been run for a fault dipping at $45°$ to the horizontal, with the maximum principal stress σ_1 which is vertical and assumed at an angle of $45°$ to the fault. These conditions are consistent with the dip of the 1997 Colfiorito earthquake fault inferred from seismological data (Chiaraluce et al., 2003), and with field observation of exhumed, natural seismic faults from our case study in the Northern Apennines of Italy (De Paola et al., 2008; Fig. 1). During the simulations, σ_1 is kept constant and equal to the lithostatic load (i.e., 175 MPa at 7 km depth). All models are run from an initial stress state with σ_3 set at 85% of lithostatic load (Miller et al., 2004).

Our simulations directly model pore pressure only within the OFC and IFC, while hydrostatic fluid pressure is imposed on all outer boundaries of the model, except for a 40 m thick overpressured section. This mimics the effect of an overpressured external reservoir hosted in the fractured dolostones of the damage zone (Fig. 2; Trippetta et al., 2013; Chiodini et al., 2004). Here, we approximate it as an infinite, permanently overpressured volume in the damage zone.

To reduce computational costs, we exploit the model's symmetry properties. The idealised fault section has two planes of symmetry, the fault parallel plane bisecting the fault, and the fault perpendicular plane bisecting the overpressure contacts. In our model,

these planes become symmetry boundaries, with the gradient of pore pressure normal to these boundaries set to zero.

The top and bottom fixed pressure boundaries maintain a hydrostatic pressure. The total domain of the numerical solution is large enough that the top and bottom boundaries do not significantly affect the pressure distribution within the nucleation area. For each simulation, the length of the simulated fault is selected such that the pressure gradient at the upper perpendicular boundary is less than 1% of hydrostatic pressure per metre.

3. Results

A series of numerical simulations have been performed for a range of initial pore pressures, at a depth of 7 km, for a fixed tectonic unloading rate in the minimum principal stress direction. Fluid flow in the fault core during the interseismic period is modelled for two end-member scenarios, Case A and B. In the simpler Case A, permeability of the OFC during the interseismic period is solely controlled by pore pressure variations and lithological factors (e.g. fabric presence and orientation; Fig. 4a-b). In the more complex Case B, permeability evolution during the interseismic period is also controlled by the deformation, associated to brittle or ductile failure in the OFC (Fig. 4c-d).

The scope of the above simulations is to investigate the effect of pore pressure evolution in the fault core on the duration of the nucleation phase and on the size of the nucleation patch, as described in the results sections below.

3.1. Pore pressure evolution and onset of failure

3.1.1. Simple Case A

During the interseismic period, permeability evolves with pore pressure variations and lithological factors in the OFC, while it is constant (but anisotropic) along the fault-parallel and -orthogonal direction in both the IFC and PSZ (Fig. 2). The pore pressure conditions in the fault zone are represented by the pore fluid factor λ_v, defined as the ratio between pore pressure and lithostatic load. We model fluid flow for two pore pressure regimes in the damage zone reservoir, with slightly supra-hydrostatic ($\lambda_v = 0.45$) and sub-lithostatic ($\lambda_v = 0.85$) initial pore pressure conditions, compared to initially hydrostatic ones ($\lambda_v = 0.4$) in the fault core (Fig. 5a, d).

At the beginning of the interseismic period, soon after an earthquake event, pore pressure excess is concentrated in the vicinity of the overpressure contact at the DZ/OFC boundary (Fig. 5a, d). High time resolution simulations show that pore fluids start to rapidly diffuse within the OFC first and then into the IFC and PSZ, where pores pressure increases along the fault-parallel and -perpendicular direction. A quasi-steady state pore pressure regime is attained in the fault zone on the order of days.

Failure by sliding along the PSZ will start at 356 and 119 years, for $\lambda_v = 0.45$ and 0.85, respectively, when the shear stress level, which is controlled by the tectonic loading rate, matches the fault strength, which is dependent on pore fluid pressure (Fig. 5g). At this time, failure patches begin to develop along the PSZ in the supra-hydrostatic and sub-lithostatic pressure cases, respectively (L_F in Fig. 5b, e).

3.1.2. Complex and more realistic Case B

We now consider the more complex and realistic scenario where permeability evolution during the interseismic period in the fault core is additionally controlled by deformation, via brittle or ductile failure in the OFC (Fig. 4c-d). We consider here the same two scenarios as before, for slightly supra-hydrostatic ($\lambda_v = 0.45$) and sub-lithostatic ($\lambda_v = 0.85$) initial pore pressure condition in the damage zone reservoir, again compared to initial hydrostatic ones ($\lambda_v = 0.4$) in the fault core (Fig. 6a, e).

Let us consider first the case of slightly supra-hydrostatic ($\lambda_v = 0.45$) initial pore pressure conditions in the damage zone reservoir, and assume the same initial state of stress in the fault and extensional tectonic unloading rate as in the previous scenario (Fig. 6i-j). Similarly to the case with no deformation control, high time resolution simulations show that pore fluids start to rapidly diffuse within the OFC first and, then, into the IFC and PSZ. After 327 years, the stress level in the OFC is such that ductile failure sweeps rapidly across its full width (Fig. 6b), before sliding begins along the PSZ (Fig. 6i-j). Sliding along the PSZ occurs earlier than in Case A (Fig. 5b, 6c), at almost the same time as ductile failure in the OFC.

For sub-lithostatic ($\lambda_v = 0.85$) initial pore pressure conditions in the damage zone reservoir, pore fluids start to rapidly diffuse within the OFC, IFC and PSZ, and pore pressure reaches a quasi-steady state after 19 days. At this time, higher pore pressure values are attained than in Case A. This means that the OFC Mohr circle is more translated to the left than in Case A and, hence, will intercept the brittle segment of the OFC failure envelope during loading (Fig. 6i-j). After 58 years, brittle failure begins in the OFC increasing its permeability by around 3 orders of magnitude (Fig. 6f). Sliding along the PSZ first occurs at 58.7 years (L_F in Fig. 6g), while the brittle failure front extends away from the overpressure contact, towards the IFC. There is no ductile failure in this case due to the lower level of effective pressure in the OFC (Fig. 6i-j). The onset of sliding along the PSZ occurs after about 59 years, earlier than in Case A when there is no-deformation in the OFC (Compare Fig. 5e and 6g).

3.2. Pore pressure evolution and earthquake nucleation

During our simulations, we assume velocity weakening behaviour for the PSZ (F in Table 1 and Eq. (3)), which has been observed for anhydrite and dolomite-rich gouge at high temperature, room humidity and sub-seismic sliding velocity (Scuderi et al., 2013), whilst experiments on water saturated with CO_2 anhydrite/dolomite mixtures show velocity-strengthening behaviour (Pluymakers et al., 2016). When shear stress exceeds the fault shear strength, for a given pore pressure, sliding begins along the PSZ. This condition coincides with the beginning of the nucleation phase, which ends when the size of the sliding patch on the PSZ equals that of the nucleation length (i.e. $L_F = L_N$ in Figs. 5c,f and 6d, h); a condition leading to the dynamic fast propagation of the rupture. Hence, the computed nucleation length values can be used to estimate the duration of the nucleation stage.

For the simple Case A, with no deformation control on permeability, our results show that the initial pore pressure within the damage zone reservoir controls the time at which sliding initiates along the PSZ (Fig. 5b, e). In fact, the nucleation phase initiates significantly earlier for sub-lithostatic ($\lambda_v = 0.85$; Fig. 5e) initial pore pressure conditions than for slightly supra-hydrostatic ones ($\lambda_v = 0.45$; Fig. 5b). During the nucleation phase of the earthquake, the failure patch grows along the PSZ until conditions for dynamic seismic rupture propagation are attained (e.g. $L_F = L_N$ in Fig. 5c, f).

Remarkably, the nucleation phase is one order of magnitude longer in the case of initial sub-lithostatic pore pressure conditions (10.1 years, Fig. 5b-c), than in the case of supra-hydrostatic ones (0.4 years, Fig. 5e-f). These results are due to the trade-off of two competing effects: the reduction of effective normal stress due to high pore pressures and the growth of the failure patch along the PSZ. The higher the pore pressure, the lower the effective normal stress so the sooner sliding can begin (Fig. 5b, e). However, the lower the effective normal stress, the higher the nucleation length so a larger sliding patch is needed for earthquake nucleation, resulting in a longer nucleation phase (Fig. 5c, f). It is worth noting
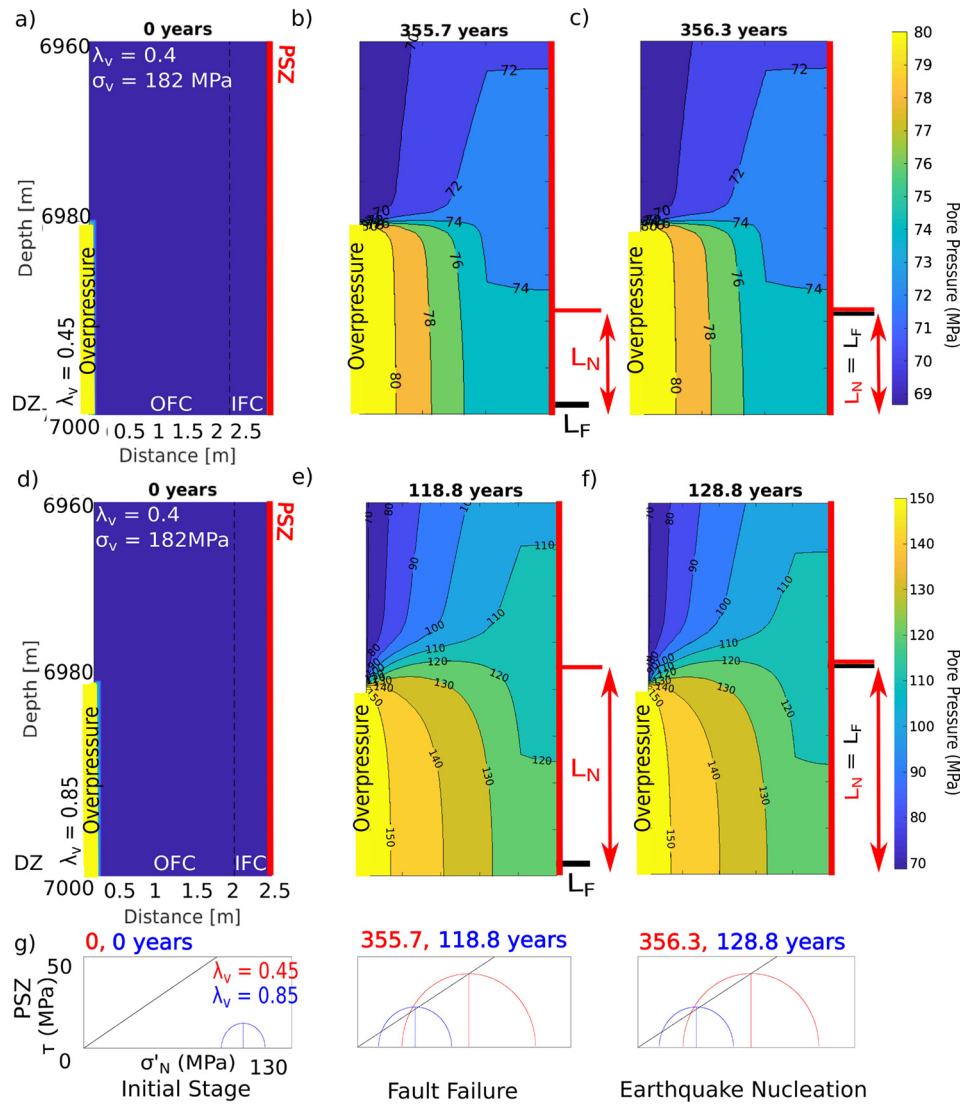
Fig. 5. Simulation results of pore pressure evolution and onset of failure – Simple Case A. a, d) Plots are provided for slightly supra-hydrostatic, $\lambda_v = 0.45$ (a), and sub-lithostatic, $\lambda_v = 0.85$ (d) initial pore pressure conditions in the damage zone reservoir, compared to initially hydrostatic ones ($\lambda_v = 0.4$) in the fault core. b, e) Pore pressure evolution from initial conditions to the time at which failure initiates in a failure patch (L_F), along the main principal slip zone (PSZ) in the inner fault core (IFC). Note that the size of the failure patch, L_F, is not to scale in these panels, as L_F is infinitesimally small at the onset of failure. c, f) Pore pressure conditions at the time an earthquake nucleates, when the size of the failure patch, L_F, matches that of the theoretical predicted nucleation length, L_N. g) Mohr failure analysis for the PSZ at initial conditions (a, d), onset of fault failure (b, e) and earthquake nucleation (c, f). Results are presented for 40 m of 1 km simulated region shown vertically, and 2.5 m fault core exaggerated horizontally.

that, during the nucleation phase, pore fluid pressure conditions do not vary from the steady state conditions attained early during the interseismic period (Fig. 5b-c, 5e-f). Hence, it is the nucleation length inverse dependence on pore pressure that controls the duration of the nucleation phase.

In Case B scenario, the occurrence of ductile ($\lambda_v = 0.45$) and brittle ($\lambda_v = 0.85$) failure before and during the nucleation phase significantly increases permeability within the OFC (Figs. 6b-d, 6f-h). The permeability enhancement caused by ductile and brittle deformation in the OFC changes the pore pressure field within the OFC and IFC. These pore pressure variations reduce the duration of the interseismic period, when compared to the case with no deformation (e.g. compare Figs. 5b, e with Fig. 6c, g). This effect is particularly significant for the initial sub-lithostatic pore pressure regime (Fig. 6e), when brittle deformation in the OFC can halve the length of the interseismic period, when compared to the case with no deformation (Fig. 5f, 6h).

The length of the nucleation phase is 0.1 years in the case of initial sub-lithostatic pore pressure conditions (Fig. 6g-h) and

much quicker, below the resolution of the modelling, in the case of supra-hydrostatic ones (Fig. 6c-d).

Compared to the case with no deformation control on permeability, transient fluid pressures conditions occur during the nucleation phase (Fig. 6c-d, 6g-h), as opposed to the quasi steady state conditions attained in the simple Case A without deformation-dependent permeability (Fig. 5b-c, 5e-f).

3.3. Pore fluid factor control

We perform parameter studies of the same two case scenarios, without (Case A) and with (Case B) deformation-dependent permeability, by running multiple simulations at a range of different pore fluid factors ($0.45 < \lambda_v < 0.85$, in steps of 0.025) (Fig. 7a-c). The procedure to obtain the duration of the interseismic period (Fig. 7a) and nucleation phase (Fig. 7c), and the length of the failure patch at nucleation (Fig. 7b) is the same as the one described as in the main text in Section 2.2.3, and in Sections 3.2 and 3.3.
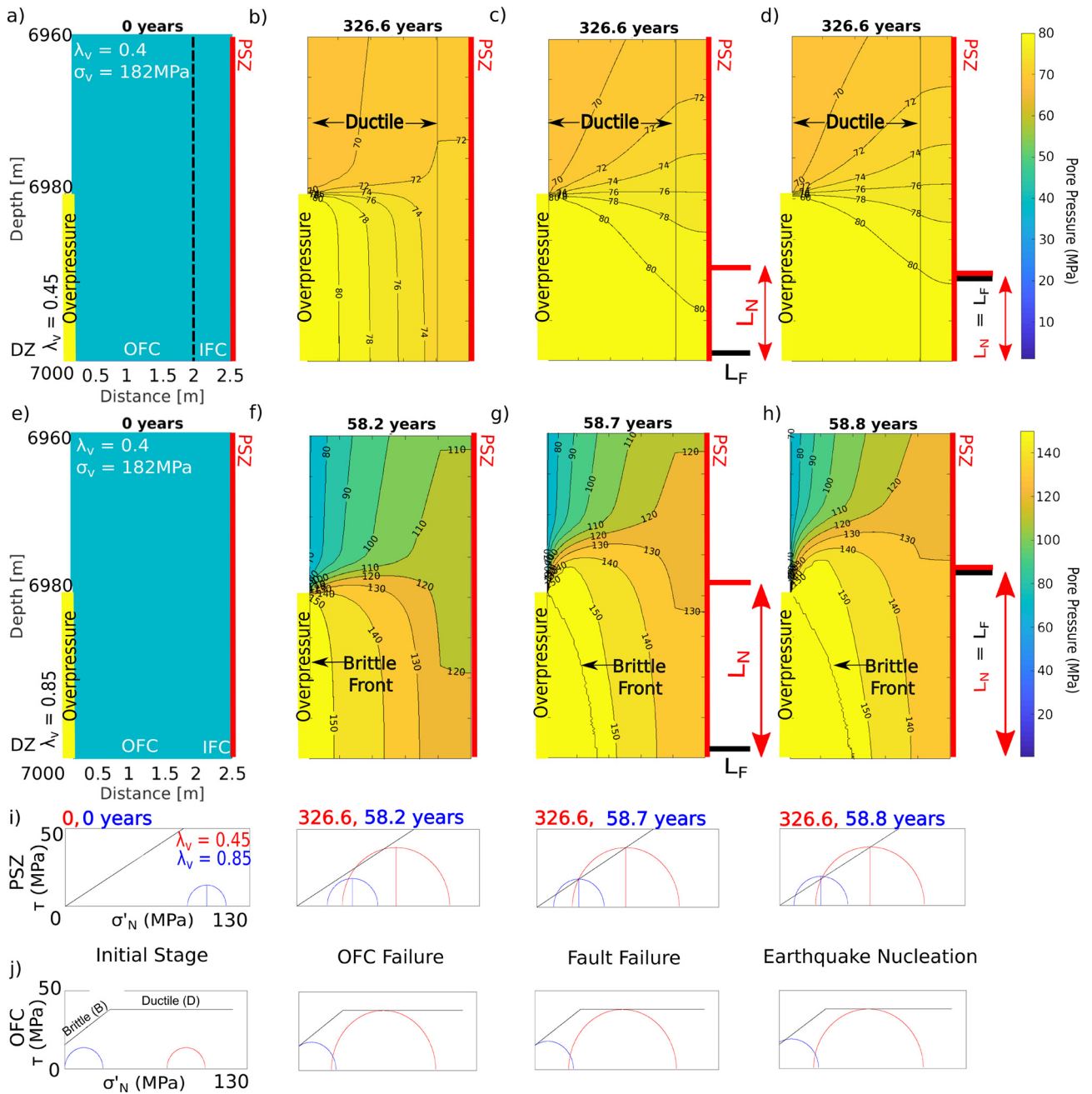
Fig. 6. Simulation results of pore pressure evolution and onset of failure – Complex and realistic Case B. a, e) Plots are provided for slightly supra-hydrostatic, $\lambda_v = 0.45$ (a), and sub-lithostatic, $\lambda_v = 0.85$ (e) initial pore pressure conditions in the damage zone reservoir, compared to initially hydrostatic ones ($\lambda_v = 0.4$) in the fault core. b, f) Pore pressure evolution from initial conditions to the time at which ductile (b) and brittle (f) failure initiates in the outer fault core (OFC). Black arrows indicate the extent of ductile and brittle deformation front in the OFC. c, g) Pore pressure conditions when fault failure initiates in a patch (L_F), along the main principal slip zone (PSZ) in the inner fault core (IFC). d, h) Pore pressure conditions at the time an earthquake nucleates, when the size of the failure patch, L_F, matches that of the theoretical predicted nucleation length, L_N. i–j) Mohr failure analysis for the PSZ (i) and OFC (j) at initial conditions (a, e), onset of ductile (b) and brittle (f) failure in the OFC, onset of fault failure (c, g) and earthquake nucleation (d, h). Results are presented for 40 m of 1 km simulated region shown vertically, and 2.5 m fault core exaggerated horizontally.

Our results show that pore fluid factor and deformation-dependent permeability all exert primary control over the duration of the interseismic period and nucleation phase, and over the length of the failure patch at nucleation. In particular, increased initial pore fluid factor in the pressurised reservoir acted in both scenarios to decrease the duration of the interseismic period (Fig. 7a), and to increase the nucleation length (Fig. 7b) and the duration of the nucleation phase (Fig. 7c).

The timing of brittle failure in the OFC is dependent on pore fluid factor, while the timing of ductile failure is constant due to the flat ductile region of the OFC failure envelope (Fig. 3a). In

all cases, the inclusion of deformation-dependent permeability decreases both the interseismic period (to 60.1 years, Fig. 7a) and the nucleation phase duration (to less than 1 year, Fig. 7c), while increasing the size of the nucleation length (to >30 m, Fig. 7b).

It is interesting to note that for pore fluid factors of 0.55 the results obtained for the two scenarios considered here converge (Figs. 7a-c). This is due to the specific tectonic loading rate chosen for our simulations, which causes fault sliding in the PSZ before any fracturing by brittle or ductile failure can occur within the OFC. This observation shows that tectonic loading rate also plays
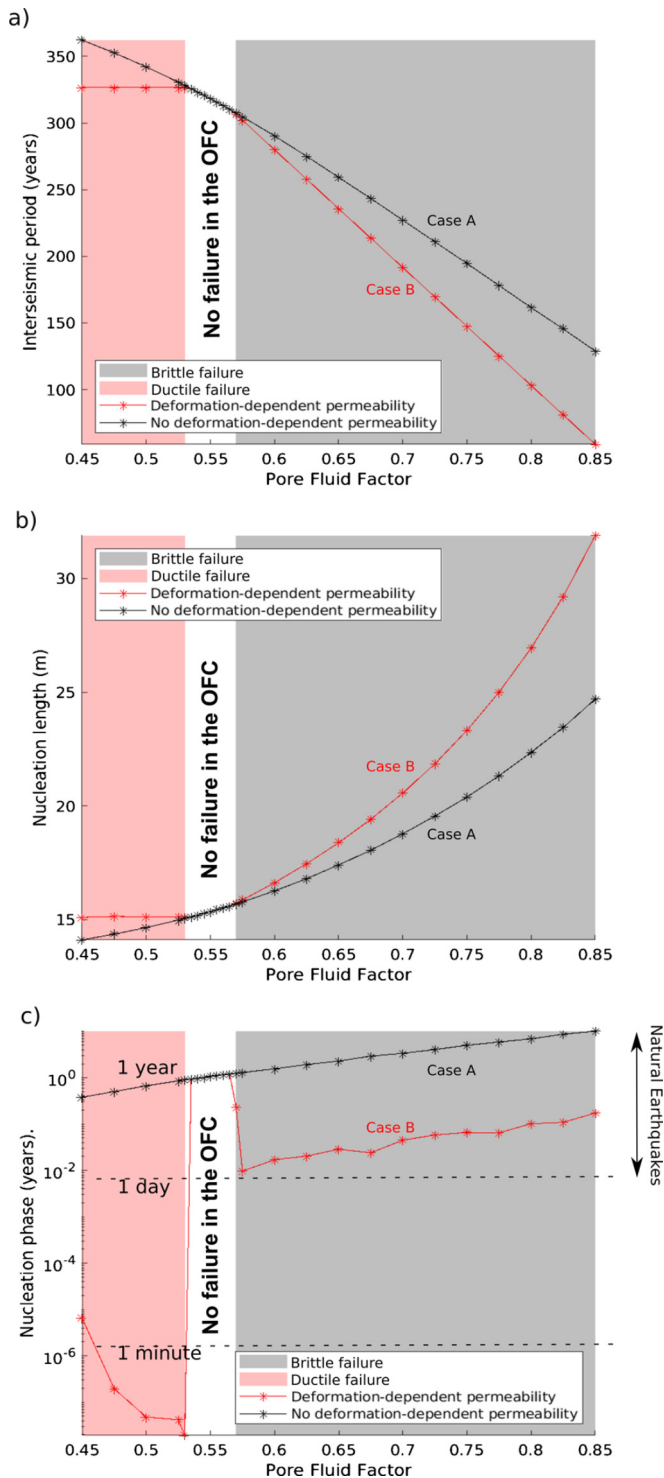
Fig. 7. Variations of earthquake parameters vs. pore fluid factor. Length of interseismic period (a), nucleation length (b) and duration of nucleation phase (c) are plotted against variation of the pore fluid factor across multiple simulations for Case A and Case B, respectively. For case B, the pressure fields of ductile and brittle deformation in the OFC are also shown in pink and grey, respectively. The white area between the brittle and ductile deformation fields corresponds to those conditions where failure along the PSZ in the IFC occurs before any deformation and failure can occur in the OFC. In the latter case, with no deformation in the OFC, the solutions for Case B converge to those for Case A obtained with no deformation. In panel 7c, a double-headed arrow also shows the range of lengths of the nucleation phase of some natural earthquakes, estimated by seismological observations (Fig. 7c; Mavrommatis et al., 2014; Kato et al., 2012; Socquet et al., 2017). (For interpretation of the colours in the figure(s), the reader is referred to the web version of this article.)

a role in controlling pore pressure diffusion in fault zones during the seismic cycle.

4. Discussion and conclusions

4.1. Mode of failure controls pore pressure diffusion and earthquake recurrence interval

Small scale fracturing within fault zones acts as a primary control on pore pressure diffusion during the interseismic period (e.g. natural earthquakes) or when a stress perturbation is caused in a reservoir (e.g. induced seismicity). In general, fracturing can increase the average permeability of rocks in the zones of damage adjacent to the main slip zones by several orders of magnitude, and therefore driving pore pressure diffusion more effectively. In the specific case investigated here, for a given tectonic fault-loading rate, failure-enhanced pore fluid diffusion within the fault core (OFC) reduces the frictional strength of the fault at a faster rate, and fault sliding (e.g. beginning of the nucleation phase) can initiate earlier than in the case where no fracturing occurs in the fault core (Fig. 7a).

More specifically, results from our case study show that initial high pore pressures can cause small scale brittle failure in the fault core during the interseismic period, which creates higher permeability than ductile failure occurring at lower initial pore pressures (e.g. Fig. 6b-c and 6f-g). Hence, in the case of brittle failure in the fault core, fault sliding occurs much earlier than in the case of failure by ductile deformation, reducing the duration of the interseismic period (Fig. 7a).

These results have implications in terms of seismic hazard estimates, as they show that local factors such as lithology and fault zone structure can significantly affect the length of the interseismic period and, hence, the recurrence interval of earthquakes. They also show that, during the coseismic and interseismic period, the evolution of the hydrogeological conditions of the fault zone and its connected reservoirs will affect the recurrence interval of events. In particular, hydrogeological monitoring of springs (e.g., Barberio et al., 2017) and boreholes in the epicentral area or in the surrounding areas of injection sites could potentially provide information on coseismic fluid discharge and on interseismic fluid recharge between the fault zone and the connected aquifers. These observations could be used to monitor pore pressure evolution of the fault zone and its surroundings during the seismic cycle.

It is worth noting here that, although our model accounts for realistic, complex fault zone architecture and laboratory derived permeability evolution with pore pressure and mode of failure during progressive deformation, it is still very simplistic. In fact, several other mechanisms and factors, such as poro-elasticity, stress transfer, dynamic friction evolution, dilation/compaction during shearing in the slip zone, will also affect pore pressure and fluid flow in fault zones, in addition to those considered in our model. Future modelling effort should implement such mechanisms and factors to produce more realistic models.

4.2. Implications for fluid induced earthquake nucleation

Our results have some implications for our understanding of the role and controls of aseismic slip during the nucleation phase preceding an earthquake. Although aseismic slip episodes have been relatively commonly observed over the last decade, until very recently the occurrence of aseismic slip as a precursor to major earthquakes was almost completely unknown (Bouchon et al., 2011). Large aseismic slip episodes have now been identified immediately preceding the recent M_w 9, 2011 Tohoku earthquake (Kato et al., 2012; Mavrommatis et al., 2014) and the M_w 8.1, 2014

Iquique earthquake (Ruiz et al., 2017; Socquet et al., 2017). It is argued that these aseismic slip events, lasting up to a few months, contribute to the triggering of earthquakes and are related to their preparatory nucleation phase (Guglielmi et al., 2015).

Overall, our results show that both the inclusion of realistic models of fault zone architecture and deformation-dependent permeability (brittle and ductile failure) control the size of the sliding patch (Fig. 7b) during earthquake nucleation and the duration of the nucleation phase (Fig. 7c).

The size of the failure patch during the nucleation phase is always larger when realistic models of fault zone architecture and deformation-dependent permeability are considered (Fig. 7b). In particular, small scale fracturing by brittle failure, occurring for initially high pore pressures, provides the largest slipping patches (>30 m in Fig. 7b). For the specific model used in this study, we use the equations detailed in the Supplementary Materials I to estimate the moment magnitude (M_0) corresponding to the nucleation phase. We obtain $M_0 \approx 10^{9.4}$ N m in the case of deformation-independent permeability, corresponding to an event of magnitude $M_w = 0.2$. For the case of deformation-dependent permeability, the moment decreases of a factor of about 6, resulting in $M_0 \approx 10^{8.6}$ N m and $M_w = -0.4$.

The estimated moment magnitude corresponding to the nucleation phase modelled in our study is in all cases very small, and below the current detection threshold of satellite radar missions. However, these results are of particular relevance when considering that technological improvements in signal/noise ratio and spatio-temporal resolution of local geodetic data are lowering the detection thresholds for measurements of aseismic slip. Kaneko et al. (2017), regarding a model of a Parkfield repeater earthquake, discuss the detection limit using a strain meter embedded in a borehole within a hundred meters from the slip zone. With a typical noise-to-signal ratio spectrum, the lower limit of strain measured is about 10^{-9} (Agnew, 1986). From the results of Kaneko et al. (2017), we can infer that the strain measurement threshold roughly corresponds to a moment of about $M_0 = 10^9$ N m, which is close to moment of aseismic slip obtained during the nucleation phase modelled in our study. Obviously, this is just an example from a quite different seismo-tectonic context; we mention it here to illustrate the order of magnitude of the detectability threshold in the context of the specific model discussed.

Our results show that the duration of the nucleation phase is significantly reduced from a few years to a few minutes (ductile failure) or a few days/months (brittle failure) when realistic models of fault zone architecture and deformation-dependent permeability are considered. Interestingly, a nucleation phase duration of few months, obtained for high values of initial pore pressure and brittle failure (Fig. 7c), is also the time scale of aseismic slip measured during the nucleation phase of some recent large earthquakes (M_w 9, 2011 Tohoku and M_w 8.1, 2014 Iquique earthquakes).

To conclude, estimates of the duration of the nucleation phase have implications for earthquake early warning systems. In fact, intermittent aseismic creep on fault patches >30 m in diameter, over a period of few days up to a few months, could be detectable well in advance of a significant seismic event, perhaps using local geodetic data.

Acknowledgements

Appendix A. Supplementary material

Supplementary material related to this article can be found online at https://doi.org/10.1016/j.epsl.2019.115869.

References

Agnew, D.C., 1986. Strainmeters and tiltmeters. Rev. Geophys. 24 (3), 579–624.

Anderson, O.L., Isaak, D.G., 1995. Elastic constants of mantle minerals at high temperature. In: Ahrens, T.J. (Ed.), Mineral Physics and Crystallography: A Handbook of Physical Constants. American Geophysical Union, Washington, DC, pp. 64–97.

Barberio, M.D., Barbieri, M., Billi, A., Doglioni, C., Petitta, M., 2017. Hydrogeochemical changes before and during the 2016 Amatrice-Norcia seismic sequence (central Italy). Sci. Rep. 7, 11735. https://doi.org/10.1038/s41598-017-11990-8.

Barchi, M., 2002. Lithological and structural controls on the seismogenesis of the Umbria region: observations from seismic reflection profiles. Boll. Soc. Geol. Ital. 121, 855–864.

Bouchon, M., Karabulut, H., Aktar, M., Özalaybey, S., Schmittbuhl, J., Bouin, M-P., 2011. Extended nucleation of the 1999 Mw 7.6 Izmit earthquake. Science 331, 877–880.

Burke, L., 2011. Carbon Dioxide Fluid-Flow Modeling and Injectivity Calculations. U.S. Geol. Surv. Sci. Investig. Rep. 2011-5083, 16 pp.

Byerlee, J., 1978. Friction of rocks. Pure Appl. Geophys. 116, 615–626.

Caine, J.S., Evans, J.P., Forster, C.B., 1996. Fault zone architecture and permeability structure. Geology 24, 1025. https://doi.org/10.1130/0091-7613(1996)024<1025:FZAAPS>2.3.CO;2.

Campillo, M., Favreau, P., Ionescu, I.R., Voisin, C., 2001. On the effective friction law of a heterogeneous fault. J. Geophys. Res. 106, 16307. https://doi.org/10.1029/2000JB900467.

Cappa, F., Rutqvist, J., 2012. Seismic rupture and ground accelerations induced by CO_2 injection in the shallow crust. Geophys. J. Int. 190, 1784–1789. https://doi.org/10.1111/j.1365-246X.2012.05606.x.

Cappa, F., Rutqvist, J., 2011. Impact of CO_2 geological sequestration on the nucleation of earthquakes. Geophys. Res. Lett. 38, 2–7. https://doi.org/10.1029/2011GL048487.

Cappa, F., Rutqvist, J., Yamamoto, K., 2009. Modeling crustal deformation and rupture processes related to upwelling of deep CO_2-rich fluids during the 1965–1967 Matsushiro earthquake swarm in Japan. J. Geophys. Res. 114, B10304. https://doi.org/10.1029/2009JB006398.

Chiaraluce, L., Ellsworth, W.L., Chiarabba, C., Cocco, M., 2003. Imaging the complexity of an active normal fault system: the 1997 Colfiorito (central Italy) case study. J. Geophys. Res. 108, 2294. https://doi.org/10.1029/2002JB002166.

Chiodini, G., Cardellini, C., Amato, A., Boschi, E., Caliro, S., Frondini, F., Ventura, G., 2004. Carbon dioxide Earth degassing and seismogenesis in central and southern Italy. Geophys. Res. Lett. 31. n/a, https://doi.org/10.1029/2004GL019480.

Collettini, C., Cardellini, C., Chiodini, G., De Paola, N., Holdsworth, R.E., Smith, S.A.F., 2008. Fault weakening due to CO_2 degassing in the Northern Apennines: short- and long-term processes. Geol. Soc. (Lond.) Spec. Publ. 299, 175–194. https://doi.org/10.1144/SP299.11.

Collettini, C., De Paola, N., Faulkner, D.R., 2009. Insights on the geometry and mechanics of the Umbria–Marche earthquakes (Central Italy) from the integration of field and laboratory data. Tectonophysics 476, 99–109. https://doi.org/10.1016/j.tecto.2008.08.013.

Cox, S.F., 2010. The application of failure mode diagrams for exploring the roles of fluid pressure and stress states in controlling styles of fracture-controlled permeability enhancement in faults and shear zones. Geofluids 10, 217–233. https://doi.org/10.1111/j.1468-8123.2010.00281.x.

De Paola, N., Collettini, C., Faulkner, D.R., Trippetta, F., 2008. Fault zone architecture and deformation processes within evaporitic rocks in the upper crust. Tectonics 27, 1–21. https://doi.org/10.1029/2007TC002230.

De Paola, N., Faulkner, D.R., Collettini, C., 2009. Brittle versus ductile deformation as the main control on the transport properties of low-porosity anhydrite rocks. J. Geophys. Res., Solid Earth 114. https://doi.org/10.1029/2008JB005967.

Detournay, E., Cheng, A.H.-D.A., 1993. Fundamentals of Poroelasticity. Compr. Rock Eng. Princ. Pract. Proj. II, pp. 113–171.

Di Luccio, F., Ventura, G., Di Giovambattista, R., Piscini, A., Cinti, F.R., 2010. Normal faults and thrusts reactivated by deep fluids: the 6 April 2009 Mw 6.3 L'Aquila earthquake, central Italy. J. Geophys. Res. 115, B06315. https://doi.org/10.1029/2009JB007190.

Ellsworth, W.L., 2013. Injection-induced earthquakes. Science 80, 341.

Evans, J.P., Forster, C.B., Goddard, J.V., 1997. Permeability of fault-related rocks, and implications for hydraulic structure of fault zones. J. Struct. Geol. 19, 1393–1404. https://doi.org/10.1016/S0191-8141(97)00057-6.

Guglielmi, Y., Cappa, F., Avouac, J., Henry, P., Elsworth, D., 2015. Seismicity triggered by fluid injection-induced aseismic slip. Science 80 (348), 1224–1227. https://doi.org/10.1126/science.aab0476.

Kaneko, Y., Carpenter, B.M., Nielsen, S.B., 2017. Nucleation process of magnitude 2 repeating earthquakes on the San Andreas Fault predicted by rate-and-state fault models with SAFOD drill core data. Geophys. Res. Lett. 44, 162–173. https://doi.org/10.1002/2016GL071569.

Kato, A., Obara, K., Igarashi, T., Tsuruoka, H., Nakagawa, S., Hirata, N., 2012. Propagation of slow slip leading up to the 2011 W w 9.0 Tohoku-Oki earthquake. Source Sci. New Ser. 335, 705–708. https://doi.org/10.1126/science.l213778.

Leclère, H., Cappa, F., Faulkner, D., Fabbri, O., Armitage, P., Blake, O., 2015. Development and maintenance of fluid overpressures in crustal fault zones by elastic compaction and implications for earthquake swarms. J. Geophys. Res., Solid Earth 120, 4450–4473. https://doi.org/10.1002/2014JB011759.

Marone, C., 1998. Laboratory-derived friction laws and their application to seismic faulting. Annu. Rev. Earth Planet. Sci. 26, 643–696. https://doi.org/10.1146/annurev.earth.26.1.643.

Mavrommatis, A.P., Segall, P., Johnson, K.M., 2014. A decadal-scale deformation transient prior to the 2011 M_w 9.0 Tohoku-oki earthquake. Geophys. Res. Lett. 41, 4486–4494. https://doi.org/10.1002/2014GL060139.

McGarr, A., Bekins, B., Burkardt, N., Dewey, J., Earle, P., Ellsworth, W., Ge, S., Hickman, S., Holland, A., Majer, E., Rubinstein, J., Sheehan, A., 2015. Coping with earthquakes induced by fluid injection. Science 80 (347), 830–831. https://doi.org/10.1126/science.aaa0494.

Miller, S.a., Collettini, C., Chiaraluce, L., Cocco, M., Barchi, M., Kaus, B.J.P., 2004. Aftershocks driven by a high-pressure CO_2 source at depth. Nature 427, 724–727. https://doi.org/10.1038/nature02251.

Mirabella, F., Barchi, M., Lupattelli, A., Stucchi, E., Ciaccio, M.G., 2008. Insights on the seismogenic layer thickness from the upper crust structure of the Umbria-Marche Apennines (central Italy). Tectonics 27, 1–15. https://doi.org/10.1029/2007TC002134.

Mitchell, T.M., Faulkner, D.R., 2008. Experimental measurements of permeability evolution during triaxial compression of initially intact crystalline rocks and implications for fluid flow in fault zones. J. Geophys. Res., Solid Earth 113, 1–16. https://doi.org/10.1029/2008JB005588.

Paterson, M.S., Wong, T.-F., 2005. Experimental Rock Deformation – the Brittle Field, 2nd ed. Springer, Berlin. ISBN 3-540-24023-3. 348 pp.

Peach, C.J., Spiers, C.J., 1996. Influence of crystal plastic deformation on dilatancy and permeability development in synthetic salt rock. Tectonophysics 256, 101–128. https://doi.org/10.1016/0040-1951(95)00170-0.

Pluymakers, A.M.H., Spiers, C.J., 2015. Compaction creep of simulated anhydrite fault gouge by pressure solution: theory v. experiments and implications for fault sealing. Geol. Soc. (Lond.) Spec. Publ. 409 (1), 107–124.

Pluymakers, A.M.H., Niemeijer, A.R., Spiers, C.J., 2016. Frictional properties of simulated anhydrite-dolomite fault gouge and implications for seismogenic potential. J. Struct. Geol. 84, 31–46.

Rinaldi, A.P., Jeanne, P., Rutqvist, J., Cappa, F., Guglielmi, Y., 2014. Effects of fault-zone architecture on earthquake magnitude and gas leakage related to CO_2 injection in a multi-layered sedimentary system. Greenh. Gases Sci. Technol. 4, 99–120. https://doi.org/10.1002/ghg.1403.

Ruiz, S., Aden-Antoniow, F., Baez, J.C., Otarola, C., Potin, B., del Campo, F., Poli, P., Flores, C., Satriano, C., Leyton, F., Madariaga, R., Bernard, P., 2017. Nucleation phase and dynamic inversion of the M_w 6.9 Valparaíso 2017 earthquake in Central Chile. Geophys. Res. Lett. 44, 10,290–10,297. https://doi.org/10.1002/2017GL075675.

Rutqvist, J., Birkholzer, J., Cappa, F., Tsang, C.F., 2007. Estimating maximum sustainable injection pressure during geological sequestration of CO_2 using coupled fluid flow and geomechanical fault-slip analysis. Energy Convers. Manag. 48, 1798–1807. https://doi.org/10.1016/j.enconman.2007.01.021.

Rutqvist, J., Cappa, F., Mazzoldi, A., Rinaldi, A., 2013. Geomechanical modeling of fault responses and the potential for notable seismic events during underground CO_2 injection. Energy Proc. 37, 4774–4784. https://doi.org/10.1016/j.egypro.2013.06.387.

Rutqvist, J., Rinaldi, A.P., Cappa, F.F., Moridis, G.J., 2015. Modeling of fault activation and seismicity by injection directly into a fault zone associated with hydraulic fracturing of shale-gas reservoirs. J. Pet. Sci. Eng. 127, 377–386. https://doi.org/10.1016/j.petrol.2015.01.019.

Scholz, C.H., 1998. Earthquakes and friction laws. Nature 391, 37–42. https://doi.org/10.1038/34097.

Scuderi, M.M., Collettini, C., Marone, C., 2017. Frictional stability and earthquake triggering during fluid pressure stimulation of an experimental fault. Earth Planet. Sci. Lett. 477, 84–96.

Scuderi, M.M., Collettini, C., 2016. The role of fluid pressure in induced vs. triggered seismicity: insights from rock deformation experiments on carbonates. Sci. Rep. 6, 24852.

Scuderi, M.M., Niemeijer, A.R., Collettini, C., Marone, C., 2013. Frictional properties and slip stability of active faults within carbonate-evaporite sequences: the role of dolomite and anhydrite. Earth Planet. Sci. Lett. 369–370, 220–232. https://doi.org/10.1016/j.epsl.2013.03.024.

Sibson, R.H., 2000. Fluid involvement in normal faulting. J. Geodyn. 29, 469–499.

Sibson, R.H.H., 1992. Implications of fault-valve behaviour for rupture nucleation and recurrence. Tectonophysics 211, 283–293. https://doi.org/10.1016/0040-1951(92)90065-E.

Socquet, A., Valdes, J.P., Jara, J., Cotton, F., Walpersdorf, A., Cotte, N., Specht, S., Ortega-Culaciati, F., Carrizo, D., Norabuena, E., 2017. An 8 month slow slip event triggers progressive nucleation of the 2014 Chile megathrust. Geophys. Res. Lett. 44, 4046–4053. https://doi.org/10.1002/2017GL073023.

Trippetta, F., Collettini, C., Barchi, M.R., Lupattelli, A., Mirabella, F., 2013. A multidisciplinary study of a natural example of a CO2 geological reservoir in central Italy. Int. J. Greenh. Gas Control 12, 72–83. https://doi.org/10.1016/J.IJGGC.2012.11.010.

Uenishi, K., Rice, J.R., 2003. Universal nucleation length for slip-weakening rupture instability under nonuniform fault loading. J. Geophys. Res. B, Solid Earth 108. https://doi.org/10.1029/2001JB001681.

Wibberley, C.A.J., Shimamoto, T., 2002. Internal structure and permeability of major strike-slip fault zones: the median tectonic line in Mie prefecture, southwest Japan. J. Struct. Geol. 25, 59–78. https://doi.org/10.1016/S0191-8141(02)00014-7.

Wong, T., Zhu, W., Wong, T., 1997. The transition from brittle faulting to cataclastic flow: permeability evolution. J. Geophys. Res., Solid Earth 102, 3027–3041. https://doi.org/10.1029/96JB03282.

Zoback, M.D., Byerlee, J.D., 1975. The effect of microcrack dilatancy on the permeability of westerly granite. J. Geophys. Res. 80, 752–755. https://doi.org/10.1029/JB080i005p00752.